

Tuning of Shape, Defects, and Disorder in Lanthanum-Doped Ceria Nanoparticles: Implications for High-Temperature Catalysis

Fabiane J. Trindade, Sergio Damasceno, Larissa Otubo, Marissol R. Felez, Daniel Z. de Florio, Fabio C. Fonseca, and Andre S. Ferlauto*



Cite This: *ACS Appl. Nano Mater.* 2022, 5, 8859–8867



Read Online

ACCESS |



Metrics & More



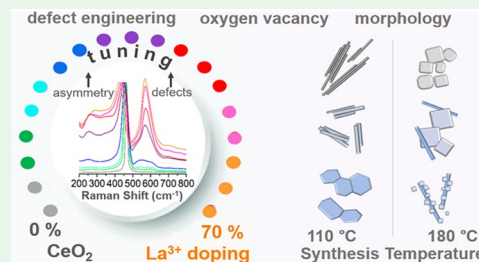
Article Recommendations



Supporting Information

ABSTRACT: The design of nanomaterials by tailoring the size, shape, and surface chemistry has a significant impact on their properties. The fine-tuning of structural defects of ceria rod-like and cube-like-shaped nanoparticles was performed via La³⁺ doping in molar ratios of 0–70 mol %. Morphology control was achieved by varying the hydrothermal synthesis temperature. For La_xCe_{1-x}O_{2-x/2} samples prepared at 110 °C, nanorod-like structures are obtained for $x < 0.30$ and a random morphology of interconnecting polyhedra is achieved for a larger x . The ceria fluorite crystalline structure is maintained at an x of up to 0.60, and both Raman and X-ray diffraction results indicate a high level of defects and disorder in the crystalline structure. For La_xCe_{1-x}O_{2-x/2} samples prepared at 180 °C, cube-shaped particles are predominant for an x of up to 0.10; however, for $x > 0.20$, two fluorite phases with different lattice parameters are associated with two distinct shapes, cubes and rods. The La concentration in nanocubes is limited to $x = 0.10$ even for samples prepared with higher nominal La concentrations, whereas the nanorods contain larger La concentrations. The demonstrated morphology and defect control on La-doped ceria nanoparticles are critical for applications such as high-temperature oxide catalysts.

KEYWORDS: cerium oxide, catalyst, doping, defect engineering, oxygen vacancy, disorder



1. INTRODUCTION

Doping of cerium oxide (CeO₂) with trivalent rare earth cations (RE³⁺) to increase its ionic conductivity has been extensively explored in several applications where efficient oxygen ion transport is paramount, such as electrolyte and electrode materials for solid oxide fuel cells,¹ permeation membranes,² and catalysis.³ Due to charge balance, the substitution of Ce atoms with 3+ cations results in excess oxygen vacancies that increase the ionic conductivity. Usually, gadolinium (Gd³⁺, 1.05 Å) and samarium (Sm³⁺, 1.08 Å) are used for doping because their ionic radii are close to that of Ce (Ce⁴⁺, 0.97 Å), resulting in high oxygen mobility. The solubility limit of these cations in the parent fluorite is 0 within a 20–30 mol % range. Higher dopant concentrations induce the C-type sesquioxide phase.^{4,5} Doping with lanthanum has been less explored because the larger difference in ionic radius (La³⁺, 1.16 Å) leads to higher lattice distortions in the fluorite structure and a lower increase in conductivity as compared to Gd and Sm.^{6,7} Recently, ceria–lanthana solid solutions (La₂Ce₂O₇) have attracted great attention as oxide catalysts for oxidative coupling of methane (OCM) reactions.^{8,9}

Lanthana has a very high solubility in the ceria fluorite structure, and more than half of Ce atoms can be replaced by La still preserving the fluorite structure. In ceria–lanthana solid solutions (La_xCe_{1-x}O_{2-x/2}), La and Ce are distributed randomly among the cationic positions, forming a disordered fluorite structure. Consequently, the distribution of oxygen

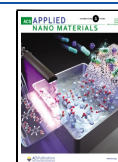
vacancies is also random within the anionic sublattice.^{10,11} For a La concentration larger than 0.50, the presence of a secondary phase with cationic ordering in a C-type superstructure has been found.¹⁰ However, the identification of C-type ordering is elusive by conventional X-ray diffraction, and less available techniques, such as pair distribution function analysis and neutron diffraction must be used to unambiguously identify such ordering. Raman spectroscopy can also be used to identify the appearance of C-type ordering.^{4,7}

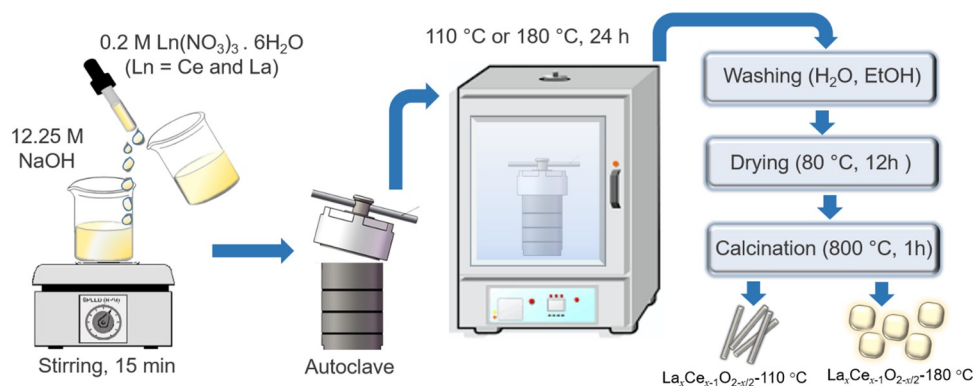
Shape control of ceria nanostructures has been widely sought, aiming mostly at catalysis applications, and hydrothermal processes using strong alkaline solution and Ce³⁺ salts such as cerium nitrate have been studied the most. In this route, experimental parameters such as temperature, anion concentration (OH⁻, NO₃⁻, etc.), and the use of capping agents, can be tuned to produce nanostructures with different shapes including rods, wires, cubes, octahedra, flowers, etc.^{12–20} The growth process can be quite complex and includes steps of nucleation, aggregation, and ripening that can be controlled and tuned depending on the synthesis

Received: March 2, 2022

Accepted: June 10, 2022

Published: June 24, 2022



Scheme 1. Representation of the Hydrothermal Synthesis of $\text{La}_x\text{Ce}_{x-1}\text{O}_{2-x/2}$ Nanoparticles

parameters. Mai et al. have shown that nanorods are preferentially formed at lower temperatures (~ 100 °C), whereas cubes are usually obtained using higher temperature (>180 °C) processes.¹² Several other studies have explored effects such as the use of excess NO_3^- concentrations for directing cubic shapes²⁰ or the use of capping agents such as oleates.¹⁵ Although many growth models have been proposed, most agree that the growth includes initial stages of oriented aggregation of small nuclei followed by dissolution and recrystallization processes that result in particle growth and consolidation. A recent review has described in detail most of the up-to-date synthesis works.¹⁹

Despite a large number of studies concerning the rare earth (RE) doping of ceria, only a few are focused on the doping of nanoparticles with a controlled shape. Rare earth elements such as Eu^{3+} , Sm^{3+} , Gd^{3+} , Tb^{3+} , and La^{3+} have been added into ceria nanocubes or nanowires,^{21–27} but usually, the RE concentration is lower than 10% and has no significant impact on the morphology. Loche et al. achieved 12% of La-doping ceria nanocubes by adding a capping agent.²⁶ Jiang et al. found a mixture of nanocubes and nanorods for Pr^{3+} doping higher than 15% without template addition.²⁷

In the present study, a systematic investigation of ceria nanoparticles doped with lanthanum prepared by the hydrothermal method was performed. Two hydrothermal conditions were chosen that yield, for pure ceria, nanorods or nanocubes. We show that La addition significantly impacts the morphology and the structural properties of the nanoparticles. Ceria nanorods can accommodate high amounts of La while keeping the fluorite phase, whereas ceria nanocubes can only accommodate $\sim 10\%$ of La. Our results provide insights into the control of disorder, defects, and shape that are crucial for the development of efficient oxide catalysts for oxidative coupling of methane reactions and catalyst support for other oxidation reactions wherein the role of oxygen species is important.

2. EXPERIMENTAL SECTION

2.1. Materials. Analytical grade lanthanum nitrate $\text{La}(\text{NO}_3)_3 \cdot 6\text{H}_2\text{O}$ ($\geq 99.9\%$, Sigma-Aldrich), cerium nitrate $\text{Ce}(\text{NO}_3)_3 \cdot 6\text{H}_2\text{O}$ ($\geq 99.9\%$, Sigma-Aldrich), and sodium hydroxide NaOH (P.A.A.C.S. 100%, Synth) were used as received without any further purification. Deionized water was used.

2.2. Synthesis of $\text{La}_x\text{Ce}_{x-1}\text{O}_{2-x/2}$. Lanthanum-doped ceria ($\text{La}_x\text{Ce}_{x-1}\text{O}_{2-x/2}$) nanostructures were synthesized in molar ratios of $x = 0; 0.05; 0.10; 0.20; 0.40; 0.50; 0.60; 0.70; 0.90$, and 1 of La^{3+} via the hydrothermal process by adaptation of a well-established protocol (Scheme 1).¹² In a typical synthesis, 19.6 g of NaOH was dissolved in

35 mL of deionized water. The nitrate salt precursors 0.2 M of $\text{Ln}(\text{NO}_3)_3 \cdot 6\text{H}_2\text{O}$ ($\text{Ln} = \text{Ce}$ and La 99.9%) in molar ratio proportions of $x = 0; 0.05; 0.10; 0.20; 0.40; 0.50; 0.60; 0.70; 0.90$, and 1 were dissolved in 5 mL of deionized and added to NaOH solution with stirring. The final NaOH concentration was 12.25 M. After stirring for 15 min, the slurry solution was transferred into a 100 mL stainless steel vessel autoclave. Next, the autoclave was heated at 110 or 180 °C in an electric oven for 24 h. After the reaction time, the system was allowed to cool at room temperature. The final product was collected by centrifugation and washed five times with deionized water and, five times with ethanol. Then, the precipitate was dried in an electric oven at 80 °C for 12 h and ground into a powder. Finally, fractions of $\text{La}_x\text{Ce}_{x-1}\text{O}_{2-x/2}-110$ °C and $\text{La}_x\text{Ce}_{x-1}\text{O}_{2-x/2}-180$ °C samples were subsequently calcined at 800 °C for 1 h.

2.3. Characterization. Scanning electron microscopy (SEM) images were obtained with a JEOL microscope FESEM JMS-6701F operated at 5 kV. The samples for SEM were prepared by drop-casting an aqueous suspension of the nanostructures over a double stick carbon tape, followed by drying under ambient conditions. Next, the 3 nm sputter platinum coating was added to improve the signal-to-noise ratio. High-resolution transmission electron microscopy (HRTEM) images were obtained with a JEOL microscope JEM 2100 operating at 200 kV. Samples for HRTEM were prepared by drop-casting an isopropanol suspension of the nanostructures over a carbon-coated copper grid, followed by drying under ambient conditions.

Nitrogen adsorption isotherms were collected with a Nova 2200 surface area and pore analyzer (Quantachrome). Specific surface areas were obtained using the Brunauer–Emmett–Teller (BET) method.

Powder X-ray diffraction (XRD) measurements were performed with a D8 Focus, Bruker AXS diffractometer, using a Ni filter, Lynxeye detector, and $\text{Cu K}\alpha$ radiation $\lambda = 1.5418$ Å. The measurements were recorded at room temperature in the $2\theta^\circ$ range varying from 10 to 90° with a step length of 0.05° at a rate of 1° min^{-1} . Since the produced samples consisted of very fine particles, no sieving was performed prior to the measurement. The structural analysis and phase identification were performed using the Rietveld method (RM) as implemented in the software TOPAS Academic 7.²⁸ The effect of instrumental peak broadening was corrected by performing a fundamental parameter (FP) function refinement of data on a strain-free micrometer-sized Al_2O_3 standard sample. For the peak profiles, a modified Thompson–Cox–Hastings pseudo-Voigt function (TCHZ function) was applied with U , V , W , and X refinable parameters.²⁹ For analysis of the size/strain, the peak shape determined for the standard sample by TCHZ was used with TOPAS macro $LVol_FWHM_CS_L$ (size) and $e0_from_Strain$ ($e0$, sgc , sgv , slc , slv) (strain). Occupancy factors were included in the case of refinement of the Ce-doped solid solutions. All parameters were refined simultaneously.

A T64000 Horiba Jobin-Yvon triple Raman spectrometer was used in the subtractive configuration with a 1024×256 OPEN-3LD/R charge-coupled device (CCD) detector for Raman scattering

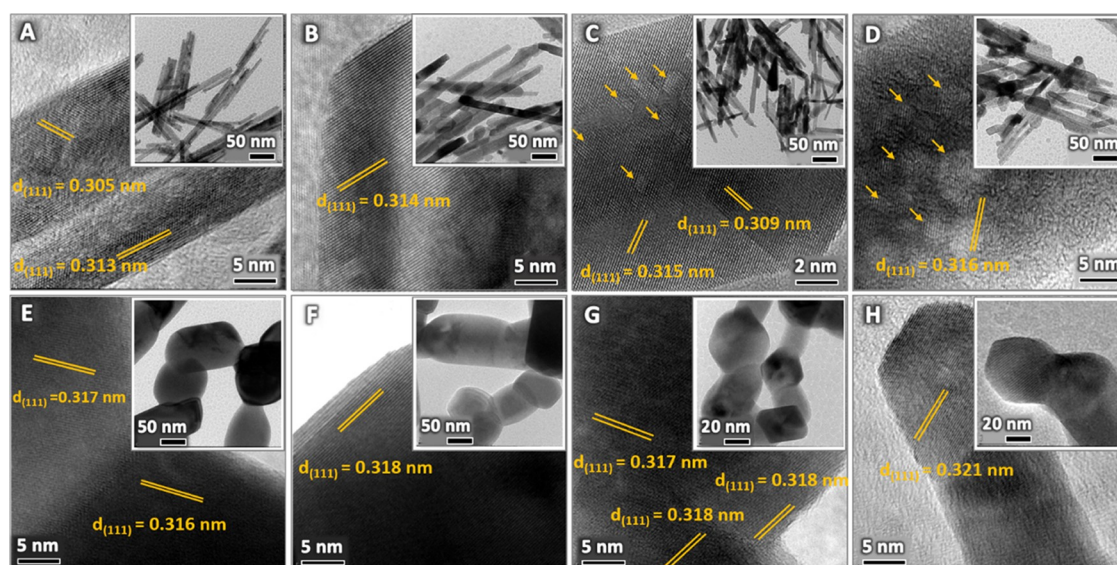


Figure 1. High-resolution transmission electron microscopy images and lower magnification images (insets) of $\text{La}_x\text{Ce}_{x-1}\text{O}_{2-x/2}$ rod-like synthesized by the hydrothermal method at $110\text{ }^\circ\text{C}$ and heat-treated at $800\text{ }^\circ\text{C}$ for 1 h: (a) $x = 0$; (b) $x = 0.05$; (c) $x = 0.10$; (d) $x = 0.20$; (e) $x = 0.40$; (f) $x = 0.50$; (g) $x = 0.60$; and (h) $x = 0.70$.

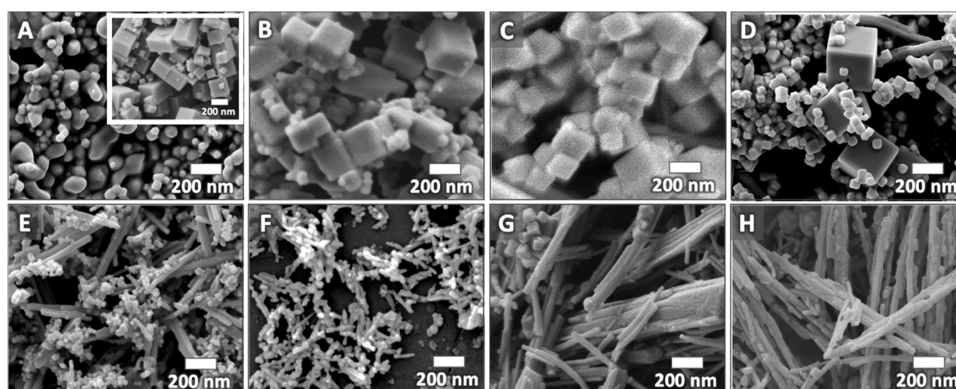


Figure 2. Scanning electron microscopy images of $\text{La}_x\text{Ce}_{x-1}\text{O}_{2-x/2}$ synthesized at $180\text{ }^\circ\text{C}$ and heat-treated at $800\text{ }^\circ\text{C}$ for 1 h: (a) $x = 0$ and the inset without heat treatment; (b) $x = 0.05$; (c) $x = 0.10$; (d) $x = 0.20$; (e) $x = 0.40$; (f) $x = 0.50$; (g) $x = 0.60$; and (h) $x = 0.70$.

measurements. The excitation laser was a Verdi G5 Laser (Coherent Inc.) operating at 532 nm (green) with a power of 2 mW on a $50\times$ objective lens.

X-ray photon electron spectroscopy (XPS) of selected samples was performed in $K\alpha$ surface analysis equipment (Thermo Scientific) with an $\text{Al } K\alpha$ X-ray source (1486.6 eV) and a flood gun. The pressure in the main chamber was $\sim 10^{-7}$ mbar. The powder samples were spread in carbon tape to minimize charging effects. For each sample, three different circular regions were investigated (diameter $\sim 300\text{ }\mu\text{m}$). For the survey spectra, 20 scans were carried out with a pass energy of 200 eV , energy step of 1.0 eV , and dwell time of 10 ms . For the individual element spectra, 10 scans were carried out with a pass energy of 50 eV , energy step of 0.10 eV , and dwell time of 50 ms . Peaks were deconvoluted using Avantage software (Thermo Scientific).

3. RESULTS

Cerium–lanthanum oxide nanoparticles, $\text{La}_x\text{Ce}_{x-1}\text{O}_{2-x/2}$, having a La^{3+} concentration, x , varying between 0 and 70 mol % were synthesized via a template-free hydrothermal process. Two series of samples were prepared using a hydrothermal temperature of 110 or $180\text{ }^\circ\text{C}$ and keeping all other synthesis parameters fixed. These temperature values were chosen because for pure ceria¹² or Gd-doped ceria CeO_2 ($x < 0.20$),²⁵ they result in the formation of CeO_2 nanorods

($110\text{ }^\circ\text{C}$) or nanocubes ($180\text{ }^\circ\text{C}$). The morphology of the nanoparticles after a heat treatment at $T = 800\text{ }^\circ\text{C}$ for 1 h, performed to ensure the formation of the desired phase, was analyzed by SEM (Figures S1 and 2) and transmission electron microscopy (TEM) (Figures 1, 3, and S2). The images reveal that La^{3+} addition significantly impacts the morphology of the obtained nanostructures. Such modifications are different in the two synthesis temperature series, $\text{La}_x\text{Ce}_{x-1}\text{O}_{2-x/2}$ - $110\text{ }^\circ\text{C}$ and $\text{La}_x\text{Ce}_{x-1}\text{O}_{2-x/2}$ - $180\text{ }^\circ\text{C}$.

As shown in Figures 1, S1, and S2, pure CeO_2 nanorods prepared at $110\text{ }^\circ\text{C}$ have an average length of 180 nm and an average diameter of 10 nm . The analysis of HRTEM images indicates that the rod's facets belong to the $\{111\}$ or $\{200\}$ plane family of the ceria fluorite structure and that the growth direction is $[110]$. Interestingly, when the lanthanum concentration is increased to $x = 0.20$, an increase in the rod diameter up to $\sim 24\text{ nm}$ is observed. Surface pit defects have been observed for samples with $x = 0.10$ and 0.20 (pointed by arrows). For $x \geq 0.40$, the well-defined rod morphology, changes to less aligned interconnected polyhedra. The average size of the polyhedra tends to reduce upon further increasing the La concentration, and interestingly for the largest $x = 0.70$,

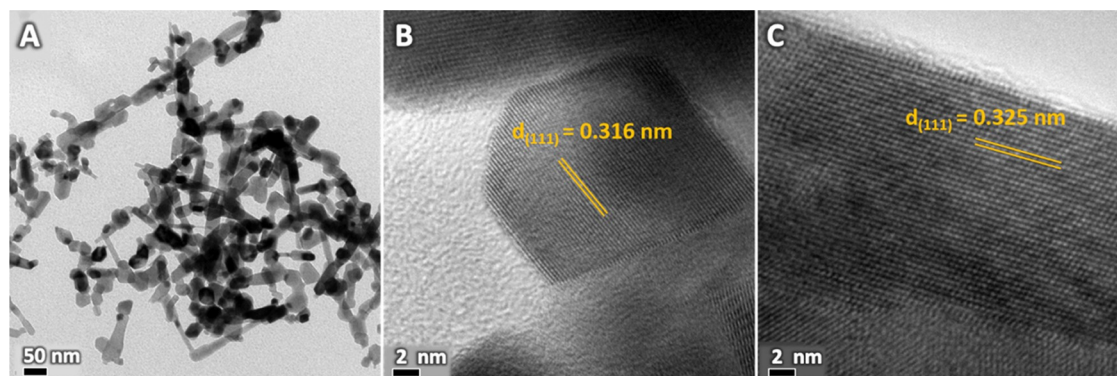


Figure 3. High-resolution transmission electron microscopy images of $\text{La}_x\text{Ce}_{x-1}\text{O}_{2-x/2}$ ($x = 0.50$) nanoparticles synthesized by the hydrothermal method at $180\text{ }^\circ\text{C}$ and heat-treated at $800\text{ }^\circ\text{C}$ for 1 h. (a) TEM image; (b) high-resolution TEM (HRTEM) image phase 1; and (c) HRTEM image phase 2.

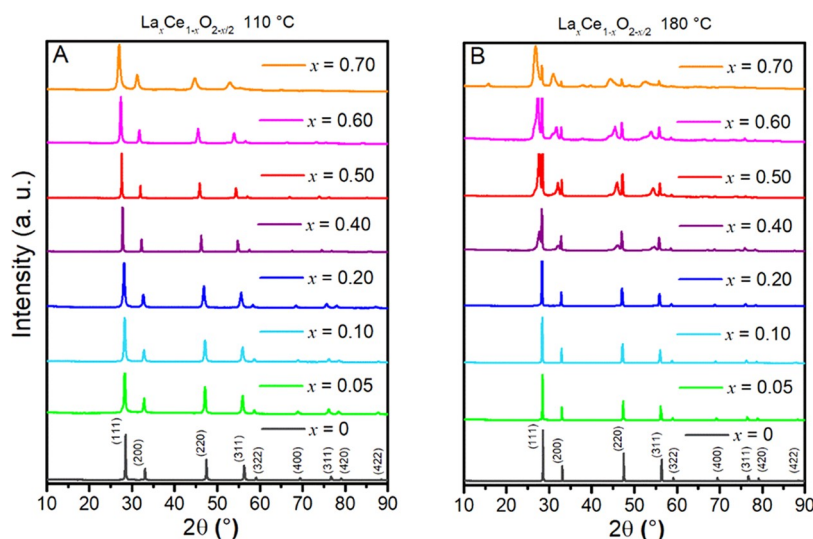


Figure 4. X-ray diffraction patterns of (a) $\text{La}_x\text{Ce}_{x-1}\text{O}_{2-x/2}$ - $110\text{ }^\circ\text{C}$ and (b) $\text{La}_x\text{Ce}_{x-1}\text{O}_{2-x/2}$ - $180\text{ }^\circ\text{C}$ samples.

the alignment between the interconnected particles is partially regained and short rod-like structures (length $< 200\text{ nm}$) are observed. The high-resolution TEM (HRTEM) images show that the interconnected nanocrystals share the $\{111\}$ planes with the same orientation indicating that oriented-attachment mechanisms are involved in the growth.

Similarly, the La^{3+} content strongly influences the nanoparticle morphology for samples synthesized at $180\text{ }^\circ\text{C}$. Figure 2 shows that undoped particles have a rounded shape. The rounding effect arises from the $T = 800\text{ }^\circ\text{C}$ annealing since the as-synthesized nanoparticles have a well-defined cubic shape (see the inset of Figure 2a). For low lanthanum concentrations, up to $x = 0.20$, the cube morphology is still prevalent; however, for $x > 0.20$, a second morphology characterized by rod-like particles is observed. These nanorods are smaller than the ones observed in the $\text{La}_x\text{Ce}_{x-1}\text{O}_{2-x/2}$ samples prepared at $110\text{ }^\circ\text{C}$ (Figure 1).

Figures 3a and S5 show a more detailed view of the nanoparticles prepared at $180\text{ }^\circ\text{C}$ for $x = 0.50$. They consist of interconnected irregular polyhedra with sizes in the $20\text{--}50\text{ nm}$ range, including some rod-like particles. In addition, Figure 3 provides examples of particles with different interplanar distances. Figure 3b shows the HRTEM image of a polyhedral particle with a low aspect ratio having an interplanar distance $d_{(111)}$ of 0.316 nm corresponding to a lattice parameter $a =$

0.547 nm . On the other hand, Figure 3c shows rod-like particles with an interplanar distance $d_{(111)}$ of 0.325 nm , with the lattice parameter $a = 0.562\text{ nm}$.

The combined HRTEM images (Figures 1 and 3–5) indicate that the formation mechanism in both hydrothermal syntheses (110 and $180\text{ }^\circ\text{C}$) involves OA mechanisms, in which smaller nuclei collide and fuse along specific crystallographic orientation¹³ resulting in either a rod-like or cube-like morphology, depending on both the temperature and the La concentration.

The successful formation and stability of the desired Ce–La solid solutions calcined at $800\text{ }^\circ\text{C}$ have been confirmed by powder XRD, as depicted in Figures 4 and S6. Upon La addition, no separate peaks corresponding to lanthanum oxide or other phases are observed up to $x = 0.60$ for $\text{La}_x\text{Ce}_{x-1}\text{O}_{2-x/2}$ - $110\text{ }^\circ\text{C}$ samples (Figure 4a), and up to $x = 0.20$ for $\text{La}_x\text{Ce}_{x-1}\text{O}_{2-x/2}$ - $180\text{ }^\circ\text{C}$ (Figure 4b). In these concentration ranges, the samples show high crystallinity, and the observed peaks correspond to the cubic fluorite structure of CeO_2 . Moreover, in the $\text{La}_x\text{Ce}_{x-1}\text{O}_{2-x/2}$ - $180\text{ }^\circ\text{C}$ series, for $x \geq 0.40$, the fluorite peak splits into a thinner peak and a broader one at lower 2θ angles (Figures 4b and S6). This effect can be attributed to the presence of two types of nanoparticles having the same fluorite structure but different lattice parameters and corroborates with the bimodal

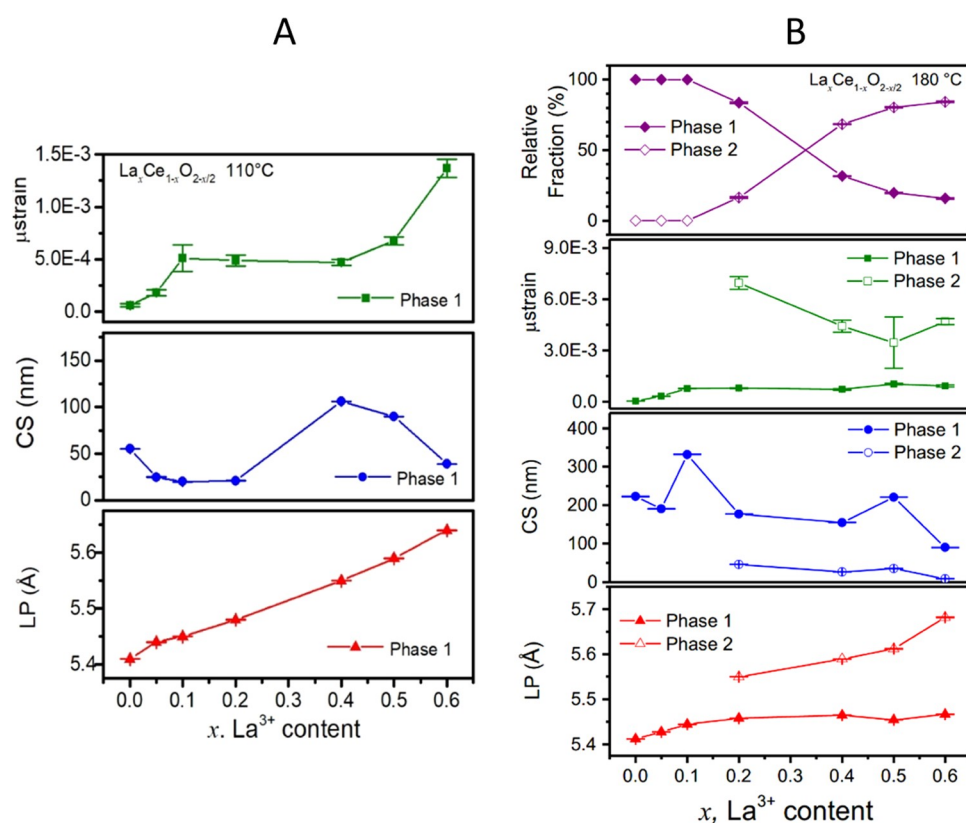


Figure 5. X-ray diffraction Rietveld analysis results. Dependence of the lattice parameter, crystallite size, and microstrain versus La³⁺ concentration for (a) La_xCe_{x-1}O_{2-x/2}-110 °C samples and (b) La_xCe_{x-1}O_{2-x/2}-180 °C samples.

morphology observed in the SEM images, and the HRTEM result of Figure 3b,c.¹⁰ Rietveld refinement was used to determine the lattice parameter of the samples, as shown in Figure 5. The increase in the lattice parameter upon La addition reflects the shift of X-ray reflections to lower angles and is associated with the expansion of the ceria lattice when increasing the lanthanum concentration, which confirms the incorporation of lanthanum into the ceria structure, resulting in a disordered cubic fluorite phase.^{3,4,8} The larger ionic radius (La³⁺ ionic radii = 1.16 Å and Ce⁴⁺ ionic radii = 0.97 Å) induces a lattice expansion, which is not counterbalanced by the reduction in O–O repulsion because of oxygen vacancy formation, which would induce a cell contraction.

For the La_xCe_{x-1}O_{2-x/2} 110 °C samples, results from the Rietveld refinement are shown only for *x* up to 0.60. The refinement indicated the presence of a single fluorite phase as expected. The presence of the hexagonal La₂O₃ phase and of the C-type sesquioxide phase was tested but their inclusion resulted in deterioration of all refinement quality parameters. On the other hand, for *x* > 0.60, the possible presence of a C-type phase and the large disorder did not allow for a statistically significant adjustment of the data (see Figure S7, Tables S1–S3). La addition results in a significant increase in microstrain, reflecting the large disorder of the structure associated with a difference in the size of cations, excess of vacancies, and random distribution of cations and anions in their sublattices. The dependence of the average crystallite size (CS) on the La content shows a curious behavior. For pure CeO₂, CS ~55 nm, and it decreases for the La content up to *x* = 0.20, after which the crystallite size increases up to CS > 100 nm (at *x* = 0.40) and then decreases back with a further increase in *x*. Such behavior reflects the changes in the

morphology, from thinner nanorods containing aligned small crystallites to consolidated polyhedra consisting of well-fused crystallites.

For the La_xCe_{x-1}O_{2-x/2} 180 °C samples, Rietveld analysis confirms the presence of two distinct fluorite phases for *x* ≥ 0.20, denoted as Phase 1 and 2 (Figure 5b). Phase 1 has a lower lattice parameter and larger crystallite size. On the other hand, Phase 2 has a larger lattice parameter and much smaller crystallite size. Phase 1 is predominant for *x* up to 0.20, but its relative fraction is continuously reduced to 15% for *x* = 0.6. A careful comparison with the morphology of the samples from the entire series indicates that Phase 1 can be associated with the cube-shaped particles, which are predominant in the low *x* samples, whereas Phase 2 comprises rod-like particles that dominate the high *x* samples (*x* > 0.50). Based on the results from the particles synthesized at 110 °C that show that the lattice parameter increases almost linearly with La concentration, one can use the lattice parameter as a gauge for the actual La concentration in the nanoparticles. Using this simple approach, it is evidenced that nanocubes contain a concentration of a maximum of *x* ~0.10, whereas the nanorods can accommodate a much larger amount of La. It is worth noting that the maximum lanthanum concentration of *x* ~0.10 estimated for the cube-like phase is similar to the limit obtained in previous studies of doped ceria nanoparticles with a cube morphology.¹⁸ On the other hand, the results from both temperature series suggest that nanorods have a porous structure that can accommodate a higher level of disorder and defects induced by higher concentrations of lanthanum. Such difference in the amount of La that can be incorporated into the different types of nanoparticles is probably due to the different growth mechanisms. Disorder and microstrain

induced by La might hinder the processes of oriented attachment and/or dissolution/recrystallization that produce large cube-like structures. Further studies would be necessary to better understand such a mechanism.

The nitrogen adsorption–desorption isotherms of $\text{La}_x\text{Ce}_{x-1}\text{O}_{2-x/2}$ samples are shown in Figure S4 and both syntheses exhibit a Type II isotherm. The textural parameters, Brunauer–Emmet–Teller (BET) surface area analysis are summarized in Table 1.

Table 1. Textural Parameters for $\text{La}_x\text{Ce}_{x-1}\text{O}_{2-x/2}$ -110 and 180 °C Heat-Treated at 800 °C for 1 h

x	BET surface area m^2/g $\text{La}_x\text{Ce}_{x-1}\text{O}_{2-x/2}$ -110 °C	BET surface area m^2/g $\text{La}_x\text{Ce}_{x-1}\text{O}_{2-x/2}$ -180 °C
0	19.44	2.30
0.05	16.59	2.75
0.10	15.76	3.58
0.20	15.32	3.44
0.40	12.42	4.89
0.50	11.60	6.75
0.60	11.42	6.17
0.70	11.31	5.73

The BET results indicate that the samples prepared at lower temperatures have a larger surface area probably because of the high porosity of the nanorods. Interestingly, for $\text{La}_x\text{Ce}_{x-1}\text{O}_{2-x/2}$ -110 °C samples, the surface area decreases with increasing La content. On the other hand, for $\text{La}_x\text{Ce}_{x-1}\text{O}_{2-x/2}$ -180 °C, it increases with the La content for x up to = 0.50. Such an increase can be attributed to the transition of a majority of cube-like particles for $x < 0.20$ to a predominance of rod-like morphological structures for $x > 0.40$.

Raman spectroscopy is a highly sensitive and effective technique to probe the disorder and the presence of defects such as oxygen vacancies in doped CeO_2 .^{4,30–35} The pure CeO_2 Raman spectrum is dominated by a strong peak at $\sim 465 \text{ cm}^{-1}$ associated with the F_{2g} vibration mode of the fluorite structure. For pure ceria, the energy position of this mode is inversely proportional to the lattice parameter, as established by the Grüneisen relation.^{4,35} In small ceria particles ($< 10 \text{ nm}$), the F_{2g} band becomes larger and asymmetric.^{32,36} This effect is attributed to phonon confinement effects that lead to a relaxation of momentum conservation.³⁷ When ceria is doped

with rare earth 3+ cations, other features in the Raman spectra become relevant. Transverse acoustic (TA) modes and transverse optical (TO) modes, which are forbidden in the fluorite structure, appear at ~ 185 and 264 cm^{-1} , respectively.³⁷ Such additional bands are assigned to disordering in the anion sublattice and develop along with a broad band covering $500\text{--}600 \text{ cm}^{-1}$ ascribed to contributions from oxygen vacancies, dopant cations, and interactions among them.^{4,36} The band at $\sim 540 \text{ cm}^{-1}$ is attributed to intrinsic oxygen vacancies, whereas the band at $\sim 600 \text{ cm}^{-1}$ is attributed to the presence of dopant–oxygen complexes.^{4,31,35}

Figure 6 shows the Raman spectra of the two series (110 and 180 °C). The red shift of the F_{2g} peak from $465\text{--}437 \text{ cm}^{-1}$ originates from the change in the lattice parameter due to the lanthanum solid solution, in perfect agreement with the XRD results. More interestingly, as the La concentration increases, the F_{2g} broadens significantly. Such broadening cannot be related to size effects because the crystallite size as determined by the XRD Rietveld analysis (Figure 5) is larger than 20 nm. It can be attributed to disorder in the lattice that induces relaxation in the momentum conservation rule due to a phonon confinement effect. Because of that, the width of the F_{2g} peak can be used to assess the disorder of the crystalline structure and a characteristic phonon correlation length can be defined as being inversely proportional to the width of the F_{2g} peak.^{30,31} This length may reflect the disorder in the position of Ce^{4+} and La^{3+} in the cationic sublattice and/or an average distance between oxygen vacancies and oxygen–dopant complexes.

In addition, Figure 7 shows a monotonic increase in the so-called defect bands at $500\text{--}600 \text{ cm}^{-1}$. In the $\text{La}_x\text{Ce}_{x-1}\text{O}_{2-x/2}$ -110 °C series, nanoparticles with a high La^{3+} concentration ($x = 0.40\text{--}0.60$) achieved a higher concentration of defects associated with oxygen vacancies and dopants (bands D_1 and D_2), as compared to $\text{La}_x\text{Ce}_{x-1}\text{O}_{2-x/2}$ -180 °C (Figure 7). Such a difference can be explained by the fact that in $\text{La}_x\text{Ce}_{x-1}\text{O}_{2-x/2}$ -110 °C, the disordered fluorite structure is maintained even at $x \sim 0.60$, whereas for the $\text{La}_x\text{Ce}_{x-1}\text{O}_{2-x/2}$ -180 °C samples, a secondary phase appears for $x > 0.20$.

In the 110 °C series a small contribution at $\sim 355 \text{ cm}^{-1}$ appears for $x \geq 40\%$. Such a peak can be assigned to the C-type ordering of the cations (Figure 6).^{2,5,8} This phase coexistence for $x \geq 0.40$ is subtle and manifests by the formation of nanodomains with C-type ordering.⁴ It is

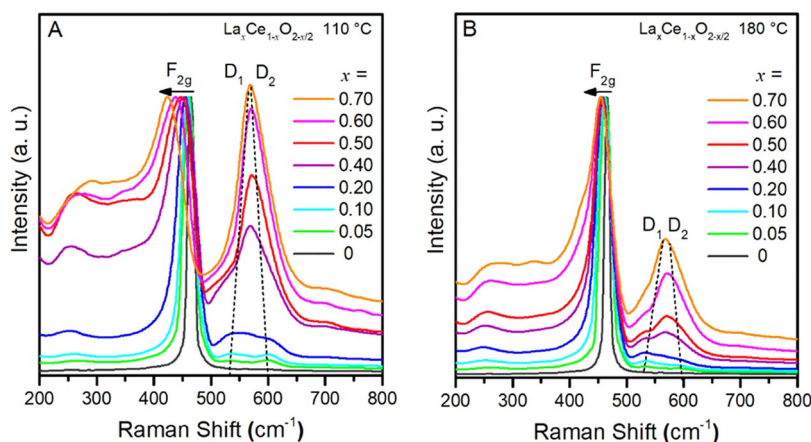


Figure 6. Raman spectra of (a) $\text{La}_x\text{Ce}_{x-1}\text{O}_{2-x/2}$ -110 °C and (b) $\text{La}_x\text{Ce}_{x-1}\text{O}_{2-x/2}$ 180 °C samples.

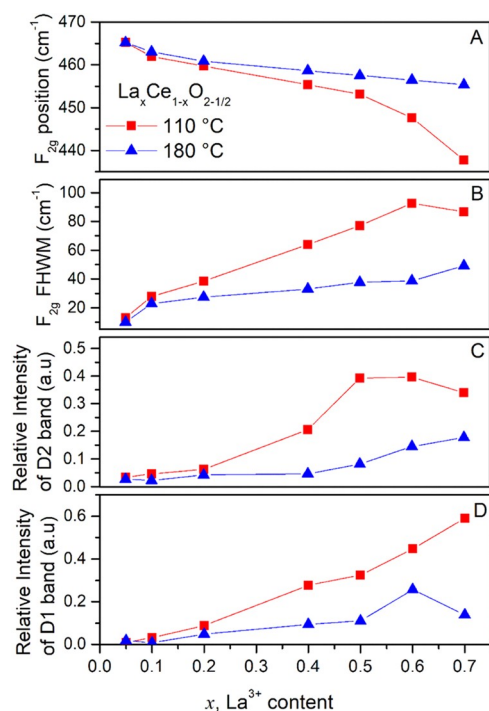


Figure 7. Results from the analysis of the Raman spectra versus La^{3+} content. (a) F_{2g} peak position; (b) F_{2g} peak width (FWHM), and (c, d) relative intensity defect bands, D_1 and D_2 , respectively.

interesting to mention that such domains have no significant effect on the XRD data for x up to 0.60 (Figures 4 and 5).

The effect of lanthanum addition on the Raman spectra of the 180 °C series is more difficult to grasp since XRD indicates the presence of two phases for $x \geq 0.20$. Thus, the observed Raman data is a sum of the contributions from the two phases. Nevertheless, they indicate that separation in the two phases results in a lower average defect concentration (lower D band) and a systematic lower amount of disorder than the corresponding nanorod samples prepared at 110 °C.

To provide a more quantitative estimation of the effect of La^{3+} addition, the Raman spectra were adjusted using a series of Lorentzian–Gaussian line shapes. The F_{2g} peak was adjusted by an asymmetric Lorentzian–Gaussian function used in CasaXP software in which exponential tails are added to a Lorentzian–Gaussian line shape. As an example, spectra of the $x = 0.50$ samples of the two series are shown in Figure S8. From the adjusted spectra, it was possible to determine the width of the F_{2g} band and the relative area of the defect band associated with oxygen vacancies (D_1) and the dopant–oxygen complexes (D_2) as compared to the normalized F_{2g} peak, shown in Figure 7c,d, respectively. These two parameters reflect the increase in lattice disorder and in oxygen vacancy concentration by increasing lanthanum concentrations, respectively. The $\text{La}_x\text{Ce}_{1-x}\text{O}_{2-x/2}$ 110 °C nanostructures achieved a much higher level of defects and disorder than the ones in the 180 °C series (Figures 6 and 7).

XPS was performed on selected samples of the two series ($x = 0, 0.10, 0.50$, and 0.70) and the Ce 3d electron peaks were adjusted to quantify the relative amount of Ce^{3+} and Ce^{4+} , following the recommendations from the work of Papparazo and references therein.^{38,39} We did not identify a clear trend associated with the La concentration in either. The relative amount of Ce^{3+} was between 22 and 34 atom % (Figure S9).

4. DISCUSSION

Next, we discuss how a variety of shapes and defects can be achieved in $\text{La}_x\text{Ce}_{1-x}\text{O}_{2-x/2}$ nanoparticles. Figure 8 provides a

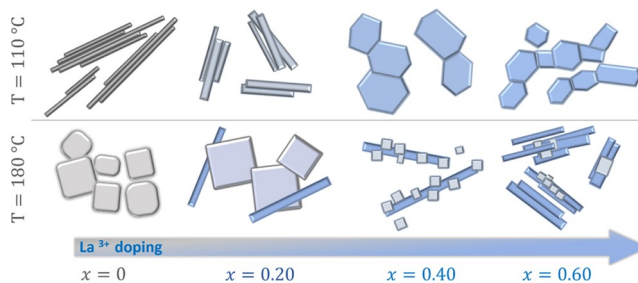


Figure 8. Schematic drawing of the morphological variation of $\text{La}_x\text{Ce}_{1-x}\text{O}_{2-x/2}$ nanoparticles as a function of the La concentration and hydrothermal synthesis temperature.

schematic drawing with a summary of the morphological variation observed. For a synthesis temperature of 110 °C, (undoped) ceria nanorods are formed with a relatively high aspect ratio (>20) and cluster in aligned bundles. La doping promotes a thickening of the rods in the low concentration range, $x = 0.05$ – 0.20 , and a reduction in the alignment of the rod-like structures within bundles. These rods are formed by OA mechanisms in which small crystalline nuclei fuse by attachment in preferential crystallographic orientation. Such a mechanism favors crystalline growth in specific directions, which explains the anisotropic shape of nanoparticles.^{13,18} HRTEM images show that the nanorod facets are preferentially the $\{111\}$ planes.

Further addition of lanthanum, $x = 0.40$ and 0.50 , imposes more disorder in the formation of the nanostructures. Larger particles are formed and have a much lower aspect ratio. TEM images show that nanoparticles tend to cluster and attach to each other, but such clustering is random and does not result in aligned structures. The XRD and Raman analyses show that these materials have a highly disordered fluorite structure that accommodates a high concentration of oxygen vacancies and dopant-related defects. The disorder in the crystalline structure is reflected in the random shape of the nanoparticles. Interestingly, for an even higher La content, $x = 0.70$, the alignment seems to return, and the rod-like shape regained, indicating that a maximum of disorder might be achieved for the samples with $x \sim 0.40$ – 0.50 .

The morphological variation in the nanoparticles prepared at 180 °C is more intricate. Pure ceria nanoparticles have a cubic shape; upon La^{3+} addition, cubes and rods coexist and, interestingly, the dependence of the morphology on the inverse of the La^{3+} concentration (see Figure 2) resembles the time sequence of growth of pure ceria cubes as observed, for example, by Dong et al.¹⁸ In their work, nanowires or rods are observed in the initial stages (which correspond to the morphology observed in our samples with higher concentrations), and then small cubic nuclei start to form and these nuclei evolve in size consuming the material from the wires. In our $x = 0.50$ sample, after 24 h of synthesis, the material is still in the nanorod formation stage, whereas in the $x = 0.40$ sample, initial cube nuclei start. For low doping levels ($x = 0.20$), the cube-shaped nanoparticles grow forming larger cubes and consuming the rod-like nanoparticles. This overall comparison indicates that the use of a higher concentration of

La nitrate in the synthesis has an effect of retardation in the growth, and similar effects were observed by Loché et al.²⁶

5. CONCLUSIONS

The experimental results show that lanthanum addition can promote significant modifications in the morphology and structural characteristics of ceria nanoparticles. The control of the final nanoparticle morphology is a result of tuning both the hydrothermal synthesis parameters and the La concentration. For the hydrothermal condition that yields CeO₂ nanorods ($T = 110\text{ }^{\circ}\text{C}$), doping with La³⁺ results in a lowering of the nanorod aspect ratio and formation of more isotropic polyhedra at high lanthanum concentrations. The CeO₂ fluorite structure in these particles can incorporate large concentrations of La³⁺ forming a solid solution of up to $x = 0.60$. At such a high concentration, the level of disorder is very large as indicated by the high values of microstrain from the Rietveld analysis and broadening of the Raman F_{2g} peaks. The oxygen vacancy concentration is also large. In contrast, under hydrothermal conditions that yield CeO₂ nanocubes (synthesis at 180 °C), lanthanum is incorporated into cube-like nanoparticles only up to $x \sim 0.10$. Further addition of La³⁺ results in a secondary phase with rod-like morphology. This phase contains the excess amount of La³⁺. Our results show that by controlling hydrothermal synthesis parameters and La³⁺ doping, ceria-based nanoparticles with tuned properties can be produced. Such control should have an important impact in high-temperature catalysis such as oxidative coupling of methane.

■ ASSOCIATED CONTENT

SI Supporting Information

The Supporting Information is available free of charge at <https://pubs.acs.org/doi/10.1021/acsanm.2c00942>.

SEM, TEM, and HRTEM images; BET isotherms; details of XRD patterns; Rietveld refinement result tables, examples of Rietveld refinement results, and examples of Raman spectra fitting; and XPS Ce 3d spectra, relative concentration of Ce³⁺ from XPS analysis, and XPS Ce 3d spectra fitting (PDF)

■ AUTHOR INFORMATION

Corresponding Author

Andre S. Ferlauto – Laboratory of Materials for Energy, Center for Engineering, Modeling and Applied Social Sciences, Federal University of ABC, 09210-170 Santo André, São Paulo, Brazil; orcid.org/0000-0003-3056-7289; Email: andre.ferlauto@ufabc.edu.br.

Authors

Fabiane J. Trindade – Laboratory of Materials for Energy, Center for Engineering, Modeling and Applied Social Sciences, Federal University of ABC, 09210-170 Santo André, São Paulo, Brazil

Sergio Damasceno – Laboratory of Materials for Energy, Center for Engineering, Modeling and Applied Social Sciences, Federal University of ABC, 09210-170 Santo André, São Paulo, Brazil

Larissa Otubo – Instituto de Pesquisas Energéticas e Nucleares, IPEN-CNEN, São Paulo 05508-000, Brazil

Marissol R. Felez – Laboratory of Materials for Energy, Center for Engineering, Modeling and Applied Social Sciences,

Federal University of ABC, 09210-170 Santo André, São Paulo, Brazil

Daniel Z. de Florio – Laboratory of Materials for Energy, Center for Engineering, Modeling and Applied Social Sciences, Federal University of ABC, 09210-170 Santo André, São Paulo, Brazil; orcid.org/0000-0002-7291-1917

Fabio C. Fonseca – Instituto de Pesquisas Energéticas e Nucleares, IPEN-CNEN, São Paulo 05508-000, Brazil; orcid.org/0000-0003-0708-2021

Complete contact information is available at: <https://pubs.acs.org/doi/10.1021/acsanm.2c00942>

Notes

The authors declare no competing financial interest.

■ ACKNOWLEDGMENTS

The authors acknowledge the Multiuser Central Facilities (Universidade Federal do ABC), and the Brazilian Nanotechnology National Laboratory (LNNano) for XPS measurements. The authors are grateful for Prof. Fabio Furlan's support in the Rietveld refinement analysis. The authors gratefully acknowledge support from the Center for Innovation on New Energies Shell (ANP)/FAPESP (2017/11937-4) and the FAPESP SPRINT project (2019/00776-5). FCF and ASF are fellows of the Brazilian CNPq.

■ REFERENCES

- (1) Jacobson, A. J. Materials for Solid Oxide Fuel Cells. *Chem. Mater.* **2010**, *22*, 660–674.
- (2) Lobera, M. P.; Serra, J. M.; Foghmoes, S. P.; Sogaard, M.; Kaiser, A. On the Use of Supported Ceria Membranes for Oxyfuel Process/Syngas Production. *J. Membr. Sci.* **2011**, *385*–386, 154–161.
- (3) Trovarelli, A. Catalytic Properties of Ceria and CeO₂-Containing Materials. *Catal. Rev.* **1996**, *38*, 439–520.
- (4) Artini, C.; Carnasciali, M. M.; Plaisier, J. R.; Costa, G. A.; Pani, M. A Novel Method for the Evaluation of the Rare Earth (RE) Coordination Number in RE-Doped Ceria through Raman Spectroscopy. *Solid State Ionics* **2017**, *311*, 90–97.
- (5) Coduri, M.; Checchia, S.; Longhi, M.; Ceresoli, D.; Scavini, M. Rare Earth Doped Ceria: The Complex Connection between Structure and Properties. *Front. Chem.* **2018**, *6*, No. 526.
- (6) Suda, E.; Pacaud, B.; Mori, M. Sintering Characteristics, Electrical Conductivity and Thermal Properties of La-Doped Ceria Powders. *J. Alloys Compd.* **2006**, *408*–412, 1161–1164.
- (7) Zamudio-García, J.; Porras-Vázquez, J. M.; Canales-Vázquez, J.; Cabeza, A.; Losilla, E. R.; Marrero-López, D. Relationship between the Structure and Transport Properties in the Ce_{1-x}XLaxO_{2-x/2} System. *Inorg. Chem.* **2019**, *58*, 9368–9377.
- (8) Xu, J.; Zhang, Y.; Xu, X.; Fang, X.; Xi, R.; Liu, Y.; Zheng, R.; Wang, X. Constructing La₂B₂O₇ (B = Ti, Zr, Ce) Compounds with Three Typical Crystalline Phases for the Oxidative Coupling of Methane: The Effect of Phase Structures, Superoxide Anions, and Alkalinity on the Reactivity. *ACS Catal.* **2019**, *9*, 4030–4045.
- (9) Zhang, Y.; Xu, J.; Xu, X.; Xi, R.; Liu, Y.; Fang, X.; Wang, X. Tailoring La₂Ce₂O₇ Catalysts for Low Temperature Oxidative Coupling of Methane by Optimizing the Preparation Methods. *Catal. Today.* **2020**, *355*, 518–528.
- (10) Coduri, M.; Scavini, M.; Brunelli, M.; Masala, P. In Situ Pair Distribution Function Study on Lanthanum Doped Ceria. *Phys. Chem. Chem. Phys.* **2013**, *15*, 8495–8505.
- (11) Kalland, L. E.; Norberg, S. T.; Kyrklund, J.; Hull, S.; Eriksson, S. G.; Norby, T.; Mohn, C. E.; Knee, C. S. C-Type Related Order in the Defective Fluorites La₂Ce₂O₇ and Nd₂Ce₂O₇ Studied by Neutron Scattering and: Ab Initio MD Simulations. *Phys. Chem. Chem. Phys.* **2016**, *18*, 24070–24080.

- (12) Mai, H. X.; Sun, L. D.; Zhang, Y. W.; Si, R.; Feng, W.; Zhang, H. P.; Liu, H. C.; Yan, C. H. Shape-Selective Synthesis and Oxygen Storage Behavior of Ceria Nanopolyhedra, Nanorods, and Nanocubes. *J. Phys. Chem. B* **2005**, *109*, 24380–24385.
- (13) Du, N.; Zhang, H.; Chen, B.; Ma, X.; Yang, D. Ligand-Free Self-Assembly of Ceria Nanocrystals into Nanorods by Oriented Attachment at Low Temperature. *J. Phys. Chem. C* **2007**, *111*, 12677–12680.
- (14) Wu, X.; Kawi, S. Synthesis, Growth Mechanism, and Properties of Open-Hexagonal and Nanoporous-Wall Ceria Nanotubes Fabricated via Alkaline Hydrothermal Route. *Cryst. Growth Des.* **2010**, *10*, 1833–1841.
- (15) Taniguchi, T.; Katsumata, K. I.; Omata, S.; Okada, K.; Matsushita, N. Tuning Growth Modes of Ceria-Based Nanocubes by a Hydrothermal Method. *Cryst. Growth Des.* **2011**, *11*, 3754–3760.
- (16) Sayle, T. X. T.; Inkson, B. J.; Karakoti, A.; Kumar, A.; Molinari, M.; Möbus, G.; Parker, S. C.; Seal, S.; Sayle, D. C. Mechanical Properties of Ceria Nanorods and Nanochains; The Effect of Dislocations, Grain-Boundaries and Oriented Attachment. *Nanoscale* **2011**, *3*, 1823–1837.
- (17) Lin, M.; Fu, Z. Y.; Tan, H. R.; Tan, J. P. Y.; Ng, S. C.; Teo, E. Hydrothermal Synthesis of CeO₂ Nanocrystals: Ostwald Ripening or Oriented Attachment? *Cryst. Growth Des.* **2012**, *12*, 3296–3303.
- (18) Dong, C.; Zhou, Y.; Ta, N.; Shen, W. Formation Mechanism and Size Control of Ceria Nanocubes. *CrystEngComm* **2020**, *22*, 3033–3041.
- (19) Xu, Y.; Mofarah, S. S.; Mehmood, R.; Cazorla, C.; Koshy, P.; Sorrell, C. C. Design Strategies for Ceria Nanomaterials: Untangling Key Mechanistic Concepts. *Mater. Horiz.* **2021**, *8*, 102–123.
- (20) Wu, Q.; Zhang, F.; Xiao, P.; Tao, H.; Wang, X.; Hu, Z.; Lü, Y. Great Influence of Anions for Controllable Synthesis of CeO₂ Nanostructures: From Nanorods to Nanocubes. *J. Phys. Chem. C* **2008**, *112*, 17076–17080.
- (21) Bezkravnyy, O.; Malecka, M. A.; Lisiecki, R.; Ostroushko, V.; Thomas, A. G.; Gorantla, S.; Kepinski, L. The Effect of Eu Doping on the Growth, Structure and Red-Ox Activity of Ceria Nanocubes. *CrystEngComm* **2018**, *20*, 1698–1704.
- (22) Fernandez-Garcia, S.; Jiang, L.; Tinoco, M.; Hungria, A. B.; Han, J.; Blanco, G.; Calvino, J. J.; Chen, X. Enhanced Hydroxyl Radical Scavenging Activity by Doping Lanthanum in Ceria Nanocubes. *J. Phys. Chem. C* **2016**, *120*, 1891–1901.
- (23) Mendiuk, O.; Kepinski, L. Synthesis of Ce_{1-x}Er_xO_{2-y} Nanoparticles by the Hydrothermal Method: Effect of Microwave Radiation on Morphology and Phase Composition. *Ceram. Int.* **2014**, *40*, 14833–14843.
- (24) Mendiuk, O.; Nawrocki, M.; Kepinski, L. The Synthesis of Ce_{1-x}Ln_xO_{2-y} (Ln=Pr, Sm, Gd, Tb) Nanocubes by Hydrothermal Methods. *Ceram. Int.* **2016**, *42*, 1998–2012.
- (25) Esposito, V.; Kabir, A.; Rosa, M.; Van Nong, N.; Rodrigues, T. S.; Rodrigues, L. N.; Machado, M. F. S.; Moraes, L. P. R.; Marani, D.; Fonseca, F. C. Tuning Diffusion Paths in Shaped Ceria Nanocrystals. *CrystEngComm* **2019**, *21*, 4025–4029.
- (26) Loche, D.; Morgan, L. M.; Casu, A.; Mountjoy, G.; O'Regan, C.; Corrias, A.; Falqui, A. Determining the Maximum Lanthanum Incorporation in the Fluorite Structure of La-Doped Ceria Nanocubes for Enhanced Redox Ability. *RSC Adv.* **2019**, *9*, 6745–6751.
- (27) Jiang, L.; Fernandez-Garcia, S.; Tinoco, M.; Yan, Z.; Xue, Q.; Blanco, G.; Calvino, J. J.; Hungria, A. B.; Chen, X. Improved Oxidase Mimetic Activity by Praseodymium Incorporation into Ceria Nanocubes. *ACS Appl. Mater. Interfaces* **2017**, *9*, 18595–18608.
- (28) TOPAS Academic V7. <http://www.topas-academic.net/> (accessed April 17, 2022).
- (29) Thompson, P.; Cox, D. E.; Hastings, J. B. Rietveld Refinement of Debye-Scherrer Synchrotron X-Ray Data from Al₂O₃. *J. Appl. Crystallogr.* **1987**, *20*, 79–83.
- (30) Weber, W. H.; Bass, K. C.; McBride, J. R. Raman Study of CeO₂. Second-Order Scattering, Lattice Dynamics, and Particle-Size Effects. *Phys. Rev. B* **1993**, *48*, 178–185.
- (31) McBride, J. R.; Hass, K. C.; Poindexter, B. D.; Weber, W. H. Raman and X-Ray Studies of Ce_{1-x}RE_xO_{2-y}, Where RE=La, Pr, Nd, Eu, Gd, and Tb. *J. Appl. Phys.* **1994**, *76*, 2435–2441.
- (32) Spanier, J. E.; Robinson, R. D.; Zhang, F.; Chan, S. W.; Herman, I. P. Size-Dependent Properties of (Formula Presented) Nanoparticles as Studied by Raman Scattering. *Phys. Rev. B* **2001**, *64*, No. 245407.
- (33) Horlait, D.; Claparède, L.; Clavier, N.; Szenknect, S.; Dacheux, N.; Ravoux, J.; Podor, R. Stability and Structural Evolution of CeIV_{1-x}Ln III_xO_{2-x/2} Solid Solutions: A Coupled μ -Raman/XRD Approach. *Inorg. Chem.* **2011**, *50*, 7150–7161.
- (34) Filtschew, A.; Hofmann, K.; Hess, C. Ceria and Its Defect Structure: New Insights from a Combined Spectroscopic Approach. *J. Phys. Chem. C* **2016**, *120*, 6694–6703.
- (35) Schmitt, R.; Nanning, A.; Kraynis, O.; Korobko, R.; Frenkel, A. I.; Lubomirsky, I.; Haile, S. M.; Rupp, J. L. M. A Review of Defect Structure and Chemistry in Ceria and Its Solid Solutions. *Chem. Soc. Rev.* **2020**, *49*, 554–592.
- (36) Zhang, F.; Chan, S. W.; Spanier, J. E.; Apak, E.; Jin, Q.; Robinson, R. D.; Herman, I. P. Cerium Oxide Nanoparticles: Size-Selective Formation and Structure Analysis. *Appl. Phys. Lett.* **2002**, *80*, 127–129.
- (37) Popović, Z. V.; Dohčević-Mitrović, Z.; Šćepanović, M.; Grujić-Brojčin, M.; Aškračić, S. Raman Scattering on Nanomaterials and Nanostructures. *Ann. Phys.* **2011**, *523*, 62–74.
- (38) Paparazzo, E. On the Curve-Fitting of XPS Ce(3d) Spectra of Cerium Oxides. *Mater. Res. Bull.* **2011**, *46*, 323–326.
- (39) Paparazzo, E. Use and Mis-Use of x-Ray Photoemission Ce3d Spectra of Ce₂O₃ and CeO₂. *J. Phys.: Condens. Matter* **2018**, *30*, No. 343003.

Recommended by ACS

New Insights into the Bulk and Surface Defect Structures of Ceria Nanocrystals from Neutron Scattering Study

Si Luo, Katharine Page, *et al.*

MAY 27, 2021
CHEMISTRY OF MATERIALS

READ 

Evaluation of the Defect Cluster Content in Singly and Doubly Doped Ceria through In Situ High-Pressure X-ray Diffraction

Cristina Artini, Marcella Pani, *et al.*

APRIL 30, 2021
INORGANIC CHEMISTRY

READ 

Density Functional Theory Investigation of the Biocatalytic Mechanisms of pH-Driven Biomimetic Behavior in CeO₂

Hongyang Ma, Judy N. Hart, *et al.*

MARCH 01, 2022
ACS APPLIED MATERIALS & INTERFACES

READ 

Strongly Bound Surface Water Affects the Shape Evolution of Cerium Oxide Nanoparticles

Adam R. Symington, Stephen C. Parker, *et al.*

JANUARY 23, 2020
THE JOURNAL OF PHYSICAL CHEMISTRY C

READ 

Get More Suggestions >